Triisopropylsilylethynyl-functionalized anthracene-based hole transport materials for efficient hybrid lead halide perovskite solar cellsb

Ece Aktas, Thi Huong Le, Michel Frigoli, Guixiang Li, Hans Köbler, Johan Liotier, Antonio J Riquelme, Antonio Abate, Renaud Demadrille, Emilio Palomares

CHEMISTRY OF MATERIALS

pubs.acs.org/cm Article

Triisopropylsilylethynyl-Functionalized Anthracene-Based Hole Transport Materials for Efficient Hybrid Lead Halide Perovskite Solar Cells

Ece Aktas, Thi Huong Le, Michel Frigoli, Guixiang Li, Hans Köbler, Johan Liotier, Antonio J. Riquelme, Antonio Abate, Renaud Demadrille,* and Emilio Palomares*

Cite This: https://doi.org/10.1021/acs.chemmater.3c02231 Read Online

ACCESS | Metrics & More | Article Recommendations | Supporting Information

ABSTRACT: The development of hole transport materials (HTMs) is a prolific area of research due to the application of these materials in various technologies such as organic light-emitting diodes (OLEDs) or perovskite solar cells (PSCs). HTMs have notably played a crucial role in the development of high-performance PSCs since in these devices, they not only ensure the collection and transport of holes to the counterelectrode but also play an important role on the device stability. In addition to the need for these materials to have good transport properties and to be easy to process, it is also of paramount importance to guarantee that their synthesis costs are reduced to allow them to be used on a large scale. In this work, we show that the use of a 9,10-bis[(triisopropylsilyl)-ethynyl]anthracene (TIPS-anthracene) moiety as a π-conjugated core, in combination with electroactive arylamine moieties, allows us to obtain new efficient HTMs in only 2 or 4 steps after recrystallization. Solar cells fabricated with the hybrid perovskite ($Cs_{0.05}FA_{0.79}MA_{0.16}Pb(I_{0.84}Br_{0.16})_3$ and these new HTMs exhibit power conversion efficiencies of up to 19.3% under AM1.5G solar illumination, which is close to the efficiency obtained with the reference compound 2,2′,7,7′-tetrakis(*N*,*N*-di-*p*-methoxyphenylamine)-9,9′-spirobifluorene (Spiro-OMeTAD) under the same conditions. Compared to other anthracene-based HTMs reported in recent years and used with perovskites of various compositions, our molecules, which are easy to prepare and purify, are more efficient.

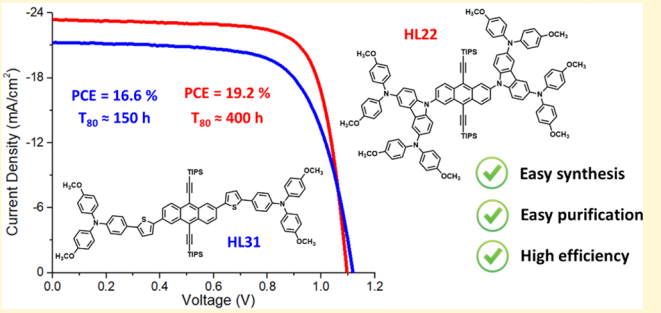

INTRODUCTION

Metal-halide perovskite materials for optoelectronic applications have developed very rapidly as a research and technology topic.[1−3] In terms of their application in photovoltaics, this has led to an extremely rapid increase in photoconversion efficiency (PCE) from 9.7% in 2012[4] to a current record efficiency of 26.1% (certified by NREL) for single bandgap devices[5] (under standard measurement conditions) and up to 33.7% (claimed at KAUST and certified by NREL)[6] for tandem devices[7] in combination with conventional silicon wafers. As perovskite solar cells (PSCs) rely on the presence of electron and hole transport layers to enhance the photogenerated charge carrier separation, the properties of these transport materials, the dynamics and interaction between the perovskite layer and these layers have attracted much attention.[8−12] The nature of the materials used for these interfacial layers can affect the overall efficiency,[13,14] the stability[15,16] or the hysteresis[17,18] behavior of the whole device. The development of new materials and the understanding of the elements involved have benefited greatly from the previous knowledge and techniques associated with more mature solar cells based on organic molecules or macromolecules such as dye-sensitized solar cells (DSSCs)[19] and organic solar cells (OSCs).[20] Focusing on the perovskite photoactive layer, the outstanding optoelectronic properties of this kind of material[21−24] responsible for these excellent results and for pushing the open-circuit photovoltage very close to their radiative limit[25] can be connected to strong ionicity of the metal−halide bond.[26,27] However, these properties can also produce chemical instability, which is one of the main drawbacks toward their full-scale implemention.[28,29] In addition, the most widely used hole selective contact, the 2,2′,7,7′-tetrakis(*N*,*N*-di-4-methoxyphenylamino)-9,9′-spirobifluorene **Spiro-OMeTAD**,[30−32] is usually doped with lithium and cobalt salts to raise its mobility[33] and with 4-*tert*-butylpyridine (tBP) to improve the layer homogeneity.[34] These additives increase the

Received: August 31, 2023
Revised: October 11, 2023
Accepted: October 17, 2023

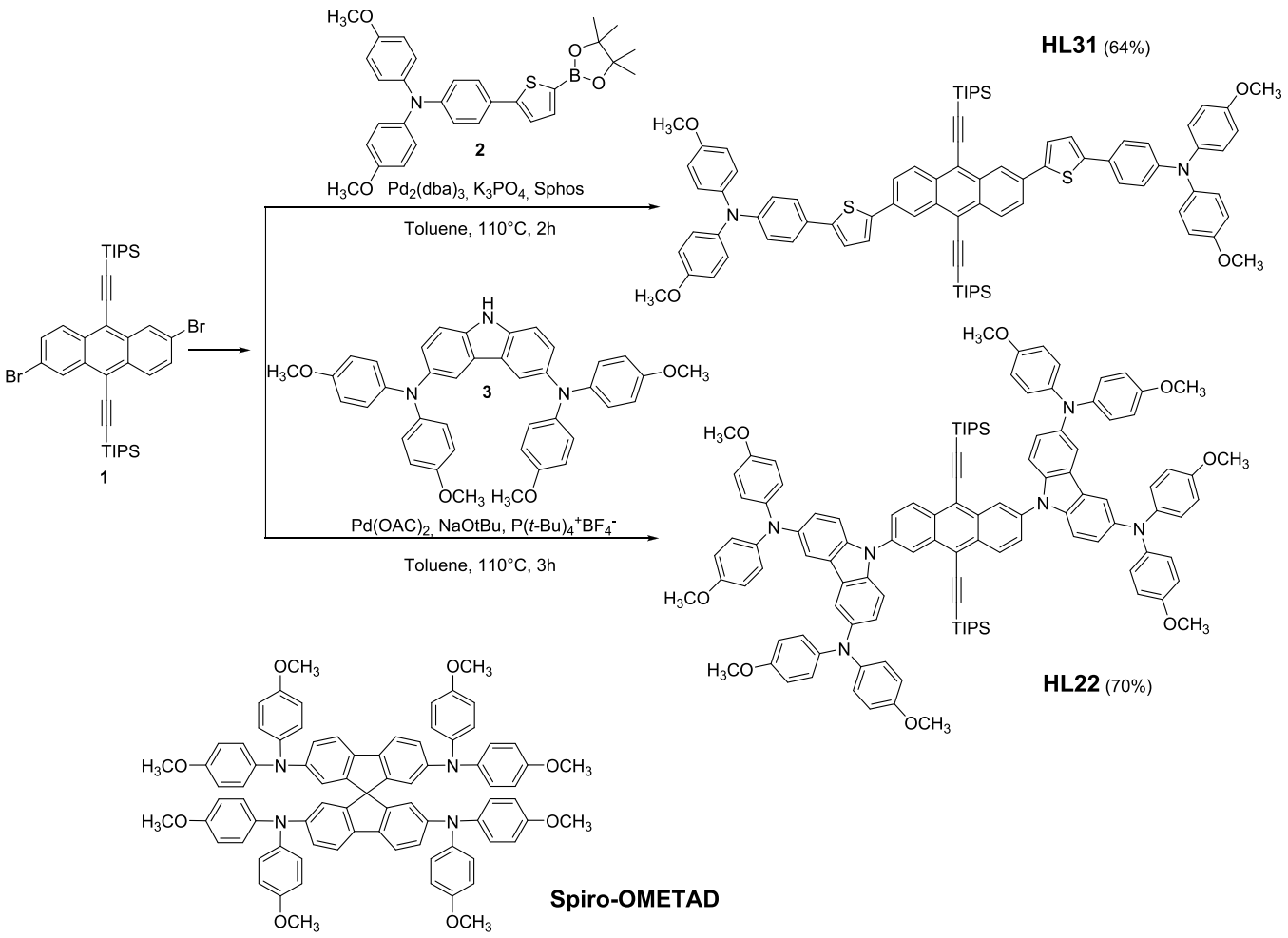

Figure 1. Summary of synthetic pathways of **HL-22** and **HL-31**. Molecular structures of **HL-22**, **HL-31**, and **Spiro-OMeTAD**.

hygroscopicity of the device, reducing its stability under ambient conditions.[35] To tackle this issue, different approaches have been used such as the encapsulation of the devices,[36,37] the development of new dopants that do not increase the hygroscopicity,[38,39] or using different deposition processes that avoid the necessity of the additives.[40] These strategies keep the **Spiro-OMeTAD** with its key role, ignoring another pressing issue regarding this material, which is the high cost of its production related to the high-purity sublimation-grade and complex multistep synthesis process required for its fabrication.[41] This has driven the scientific community to report a variety of new HTMs,[42−46] although only a handful of these options can match or exceed the record efficiencies of **Spiro-OMeTAD**.[30,47] Semiconducting polymers such as polytriarylamine[35,48] or polythiophene[49] have shown high solar-to-energy conversion efficiencies. However, polymeric materials have some drawbacks. Their synthesis and purification are not reproducible, resulting in batches with different macromolecular parameters and therefore different properties. They also often have low solubility, resulting in poor film formation and infiltration into the nanostructured material. These reasons have led to the development of small molecules as HTMs.[50−52] The main requirements for small molecules to be used efficiently as HTM in perovskite solar cells are[32] (i) a favorable energy alignment between the HOMO energy level of the HTM and the valence band of the perovskite, (ii) high mobility for hole transport to facilitate hole conduction and prevent charge recombination, (iii) high solubility in an organic solvent such as toluene or chlorobenzene, (iv) smooth and pinhole-free morphology, and (v) good thermal, moisture, and chemical stability. Among the plethora of small molecules[53] developed in the past decade only few are based on anthracene cores.[54] Anthracene is a highly planar moiety previously used to prepare emitting materials and hole or electron-transporting materials with high carrier mobility and stability,[55] applicable in organic light-emitting diodes (OLEDs).[56] This moiety is quite versatile and stable[57] and it has also been employed as an electron-rich core to prepare donor materials or for bulk heterojunction organic solar cells[58] and, more recently, nonfullerene acceptors.[59] In 2017, Dai and co-workers[54] demonstrated the potential of anthracene-based HTMs in perovskite solar cells by achieving a PCE above 15%. In 2020, Tao et al. developed hole-transporting materials, composed of *N*3,*N*6-bis(di-4-anisylamino)-9*H*-carbazole and anthracene connected in the 2,6 position, and they demonstrated better hole mobility and hole-extraction ability compared to **Spiro-OMeTAD** in perovskite solar cells.[59] By doping their anthracene-based HTMs, they achieved a PCE of 18.65%. Furthermore, they showed that PSCs based on these HTMs have a negligible hysteresis and relatively good stability. Compared to native anthracene, anthracene functionalized with TIPS-acetylene groups (TIPS-anthracene) at positions 2 and 6 significantly increases not only the solubility and hydrophobicity but also

https://doi.org/10.1021/acs.chemmater.3c02231
Chem. Mater. XXXX, XXX, XXX−XXX

the stability of these molecules. Introducing classical donors at positions 9 and 10 in TIPS-anthracene used in HTM design could provide efficient HTMs for perovskite solar cells and be obtained in a straightforward manner. Therefore, herein, we designed two TIPS-anthracene derivatives for use as HTMs in hybrid lead-based perovskite solar cells. We report their synthesis and optoelectronic properties and their advanced characterization and performances in perovskite solar cells, based on $(Cs_{0.05}FA_{0.79}MA_{0.16}Pb(I_{0.84}Br_{0.16})_3$ perovskite,[60−62] which were compared with those of **Spiro-OMeTAD** (Figure 1).

EXPERIMENTAL SECTION

Synthesis of the TIPS-Anthracene HTMs. All reactions were carried out under argon. Toluene was distilled over Na/benzophenone and kept over activated 3 Å molecular sieves. All of the commercial reagents were used without further purification. ^{1}H and ^{13}C NMR spectra were recorded at room temperature on a Bruker Avance-300 MHz NMR spectrometer. ^{1}H NMR spectra were recorded at 300 MHz and ^{13}C NMR spectra were recorded at 75 MHz. Dichloromethane residual peak was taken as an internal reference at 5.30 ppm for ^{1}H NMR and 53.52 ppm for ^{13}C NMR. High-resolution mass spectra were obtained by using a Waters Xevo Q-Tof using positive mode. Compounds **1**[63] and **2**[64] were synthesized according to the literature routes. Compound **3** in the synthetic scheme was purchased from TCI.

Synthesis of HL-22. To a bicol flask, compound **1** (100 mg, 0.15 mmol, 1 equiv), compound **3** (274 mg, 0.72 mmol, 2.5 equiv), and NaOtBu (55 mg, 0.57 mmol, 4 equiv) were added under argon followed by toluene (10 mL). The mixture was degassed for 15 min under an ultrasound with argon. Then, $Pd(OAc)_2$ (3.4 mg, 0.019 mmol, 0.1 equiv) and $P(t\text{-}Bu_3)_4{}^+BF_4{}^-$ (8.7 mg, 0.0015 mmol, 0.2 equiv) were then added to the solution. The reaction was heated to 115 °C and stirred for 3 h, reaction monitored by TLC. After returning to room temperature, the solution was filtrated through a pad of silica gel and then concentrated. The crude product was purified by column chromatography by using PE/DCM as an eluent (50/50 to 20/80). The resulting solid was first heated in methanol and then filtered. The solid was then recrystallized in a dichloromethane (DCM)/pentane mixture to provide the target molecule as brown needle-shape crystals. (180 mg, 70%). ^{1}H NMR (300 MHz, CD_2Cl_2) δ = 8.90 (s, 2H), 8.84 (d, J = 9.2, 2H), 7.93 (dd, J = 9.2, 2.1, 2H), 7.75−7.36 (m, 8H), 7.14 (dd, J = 8.9, 2.2, 4H), 6.98 (d, J = 8.5, 16H), 6.78 (d, J = 8.5, 16H), 3.75 (s, 24H), 1.33−1.05 (m, 42H); ^{13}C NMR (75 MHz, CD_2Cl_2) δ = 155.10, 137.06, 133.06, 129.37, 124.92, 124.68, 124.65, 124.57, 124.34, 118.55, 114.58, 110.90, 106.26, 102.69, 55.52, 18.79, 11.54; HRMS (TOF MS ESI+) calcd. for $C_{116}H_{116}N_6O_8Si_2 + H^+$: 1777.8471 $[M+H^+]^+$, found: 1777.8468.

Synthesis of HL31. To a bicol flask were added K_3PO_4 (360 mg, 1.73 mmol, 6 equiv) and water (1 mL) under argon. When K_3PO_4 was dissolved, toluene (9 mL) is added followed by compound **1** (200 mg, 0.29 mmol, 1eq) and compound **2** (370 mg, 0.72 mmol, 2.5 equiv). The mixture was degassed for 15 min under ultrasound with argon. Then, $Pd_2(dba)_3$ (27 mg, 0.03 mmol, 0.1 equiv) and S-Phos (24 mg, 0.06 mmol, 0.2 equiv) were added. The reaction was heated to 110 °C and stirred for 2 h. After returning to room temperature, the solution was filtered through a pad of silica gel and then concentrated. The crude product was purified by column chromatography using as eluent EP/DCM (40/60 to 20/80). The solid obtained was recrystallized in a small volume of toluene to give the target molecule as a red solid (240 mg, 64%). R_f (EP/DCM, 40/60) = 0.15; ^{1}H NMR (300 MHz, CD_2Cl_2) δ = 8.80 (s, 2H), 8.59 (d, J = 9.1, 2H), 7.91 (dd, J = 9.1, 1.8, 2H), 7.51−7.42 (m, 6H), 7.23 (d, J = 3.8, 2H), 7.08 (d, J = 8.4, 8H), 6.93−6.83 (m, 12H), 3.78 (s, 12H), 1.32−1.31 (2s, 42H);^{13}C NMR (75 MHz, CD_2Cl_2) δ = 156.26, 144.76, 141.49, 140.31, 127.67, 126.85, 126.01, 125.79, 125.09, 122.64, 122.05, 119.91, 114.64, 55.35, 18.71, 11.51; HRMS (TOF MS ESI+) calcd. for $C_{84}H_{88}N_2O_4S_2Si_2 + H^+$: 1309.5802 $[M+H^+]^+$, found: 1309.5790.

Cyclic Voltammetry (CV). CV was performed with a BAS Electrochemical system in a three-electrode single compartment cell with a glassy carbon working electrode, a coiled platinum wire counter electrode, and an $Ag/AgNO_3$ reference electrode. CV was recorded using 1−2 mM in 0.1 M $Bu_4N.PF_6$ /DCM using a scan rate of 100 mV s^{-1}. HOMO energy level was determined by E_{HOMO}= −(4.8 + $E_{1/2}{}^{Ox1}$).

Density Functional Theory Calculations (DFT). The DFT calculations were performed with the ADF suite. The geometry was optimized first with the revPBE functional and a tz2p base. To analyze the molecular orbitals with more precision, a single point was performed with the hybrid B3LYP functional (tz2p base).

Absorption Measurements. Absorption spectra were measured using 1 cm path length quartz cells in a Shimadzu UV spectrophotometer 1700 with an optical range from 190 to 1100 nm at room temperature. All the measurements were performed using toluene as solvent. The fluorescence spectra in solution were also recorded using 1 cm path length quartz cuvettes in Spectrofluorimeter Fruorolog from Horiba Jobin Yvon Ltd. with PMT (UV−vis) and InGaAs (NIR) detectors that allow fluorescence measurements in the wavelength range from 250 to 1600 nm at room temperature. The energy of the optical bandgap was calculated accordingly to E_g = 1240/$\lambda_{a.e.}$, where $\lambda_{a.e.}$ was the absorption edge wavelength onset, and its value was taken from the intersection of the normalized absorption and emission spectra recorded in diluted solutions.

Thermogravimetric Analysis (TGA). The measurements were carried out in TGA/SDTA851 Mettler Toledo equipment. The working temperature went from 30 to 600 °C at a scan rate of 10 °C/min under a nitrogen atmosphere. The decomposition temperature was considered when the samples lose up to 5% of its initial weight.

Differential Scanning Calorimetry (DSC). DSC analysis was measured in a DSC822e Mettler Toledo calorimeter. The working temperatures went from 30 to 450 °C performing three continuous cycles, at a scan rate of 10 °C/min. The glass transition temperatures for the investigated compounds were determined during the second and third heating scans under a nitrogen atmosphere.

Time-Correlated Single Photon Counting Measurements (TCSPC). Lifetime measurements were performed on an Edinburgh Instruments LifeSpec-II based on the TCSPC technique, equipped with a PMT detector, double subtractive monochromator, and 470 nm picosecond pulsed diode lasers source. All perovskite films were protected with PMMA to perform measurements in ambient conditions.

Space-Charge Limited Current (SCLC). The charge carrier mobility of HSLs was measured by the SCLC method. SCLC method was applied to only p-type materials sandwiched between the contacts. The device structure is basically ITO/PEDOT:PSS/HSL/Au. The current density−voltage curve was measured, and the concentration of charge carriers and the electric field in the device were estimated by the mobility of the holes, instead of by the recombination of the holes. The measured data is fitted in the SCLC regime using Mott−Gurney law and shown in Figure S10 and eq 1.

$$J_{SCLC} = \frac{9}{8}\varepsilon_0\varepsilon_r\mu\frac{V_{eff}}{d^3} \quad (1)$$

Here, μ is the mobility of HSL, d is the thickness of HSL, V_{eff} is the effective voltage and has a $\varepsilon_0\varepsilon_r$ value of 3 for organic semiconductors, according to the literature. The HSL thickness is usually fixed around 100 nm and the films are deposited via spin-coating. The PEDOT:PSS layers are deposited onto cleaned and treated ITO substrates via spin coating at 3500 rpm for 30 s and annealed at 130 °C for 30 min. The data were recorded with a Keithley 2612A instrument by sweeping from 1 to 5 V at a scan rate of 40 mV/s.

Current Density−Voltage Scan (*J*−*V*). The photovoltaic measurements were carried out by using 450 W xenon light source (Oriel). The spectral mismatch between AM 1.5 G and the simulated illumination was reductive by the use of a Schott 113 Tempax filter (Präzisions Glas & Optik GmbH). The light intensity was calibrated with that Si photodiode equipped with an IR cuttoff filter (KG3, Chott) and it was recorded during each measurement. Current

https://doi.org/10.1021/acs.chemmater.3c02231
Chem. Mater. XXXX, XXX, XXX−XXX

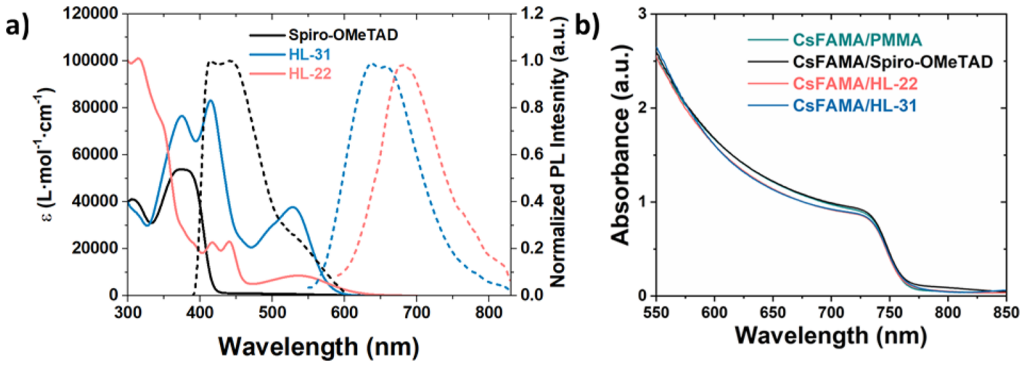

Figure 2. (a) UV−visible (solid lines) and fluorescence emission (dashed lines) spectra for **Spiro-OMeTAD**, **HL-22** and **HL-31** under standard measurement conditions in DCM. (b) Recorded spectra for the respective organic thin films onto the CsFAMA perovskite film.

voltage characteristics of the cells were obtained by applying an external voltage bias while measuring the current response with a digital source meter (Keithley 2400). The voltage scan rate was 40 mV s^{-1}. The cells were masked with a black metal mask (0.09 cm^2) to estimate the active area and reduce the influence of scattered light.

Scanning Electron Microscope (SEM). Cross-sectional images of complete devices and the perovskite surface of modified ITO were recorded using an ESEM system FEI Quanta 600 in low vacuum (0.68 Torr) with an accelerating voltage of 20 kV.

Maximum Power Point (MPP) Tracking of Perovskite Solar Cells. A custom-built High-throughput Aging Setup was used for the aging test of perovskite solar cells.[68] Each cell was individually MPP-tracked by the use of special electronics. A perturb and observe[69] algorithm with a voltage step-width of 0.01 V and a delay time of 1 s was applied to track the MPP. PCE MPP tracking values were automatically recorded for all cells every 2 min and normalized to the start value. During the tracking, the active area was touching a heat pad in order to ensure direct thermal coupling, and Peltier elements were used for cooling and kept the cells at 25 °C at all time. MPP tracking of devices was performed without encapsulation and under a continuous flow of nitrogen in a closed box. The light source intensity was actively controlled using a silicon irradiation-sensor, which itself was calibrated using a Silicon reference from Fraunhofer ISE. The aging test was in accordance with the ISOS-L-1l protocol. The UV-induced degradation was carried out with a Vilber Lourmat VL-6.L lamp. The power of the UV tube was 6 W. All HSL-deposited ITO substrates had been exposed to 365 nm for 30 min before perovskite deposition.

Device Fabrication. *Transparent Conducting Oxides Covered Glass Substrates Cleaning.* The patterned fluorinated tin oxide (FTO)-coated glass substrates are cleaned for 15 min with Mucasol 2% solution in deionized water, acetone, and isopropanol in an ultrasonic bath at 50 °C. After physical cleaning, the cleaned substrates are dried well before being treated in an UV plasma cleaner for 15 min. After UV plasma treatment, the FTO covered substrates immediately are use in the next step and they are transferred to a hot plate for depositing the compact titanium dioxide (TiO_2) layer.

Compact TiO_2 (c-TiO_2) Layer by Spray Pyrolysis. A compact TiO_2 layer was deposited by aerosol spray pyrolysis, using oxygen as a carrier gas. The precursor solution of the compact TiO_2 was prepared using 0.480 mL of acetylacetone, 0.720 mL of $(Ti(iPrO)_2(acac)_2)$ (75 wt % in isopropanol), and 10.8 mL of ethanol absolute. The total amount (12 mL) of the precursor solution was sufficient for 18 substrates. After UV plasma treatment, the substrates are heated to 450 °C and kept at this temperature for 15 min. When the deposition of the compact TiO_2 is finished by aerosol spray pyrolysis, the substrates are sintered at the same temperature for 30 min. The whole precursor solution was sprayed from the substrates at a distance of 20 cm with an inclination of 45°, with at least 20 s of delay between each spray cycle.

Mesoporous TiO_2 (m-TiO_2) Layer by Spin-Coating. The m-TiO2 was deposited on top of the c-TiO_2 by spin-coating at 4000 rpm for 10 s and 2000 rpm acceleration. The solution of the TiO_2 paste (30 nrd) was prepared using 0.3 g per 2 mL of absolute ethanol (125 mg/mL) and the paste was well dissolved under stirring. The dispersed solution of the mesoporous TiO_2 should be prepared at least 1 day before using and can be kept under stirring all the time. The coated substrates are preannealed at 100 °C for 5 min right after the spin-coating process. Then, the preannealed substrates are transferred into a hot plate and sintered at 450 °C for 30 min. The final thickness of the mesoporous TiO_2 was around 150−200 nm.

Lithium Surface Treatment by Spin-Coating. Lithium bis-(trifluoromethanesulfonyl)imide (LiTFSI) was deposited onto the mesoporous TiO_2 covered substrates for treatment just before the deposition of the perovskite layer. The LiFTSI layers are coated by spin-coating at 3000 rpm for 10 s. and 1000 rpm acceleration. The coated substrates are preannealed at 100 °C for 5 min right after the spin-coating process. Then, the preannealed substrates are transferred into a hot plate and sintered at 450 °C for 30 min.

CsFAMA Perovskite Deposition for the n-i-p Structure. The perovskite solar cells are based on CsFAMA $[(Cs_{0.05}FA_{0.79}MA_{0.16}Pb(I_{0.84}Br_{0.16})_3]$ that was prepared with an antisolvent deposition technique for n-i-p configuration. First, $PbBr_2$ (1.5 M) and PbI_2 (1.5 M) are dissolved in a mixture of anhydrous dimethylformamide (DMF):dimethyl sulfoxide (DMSO) (4:1 volume ratio) and added to formamidinium iodide (1.09:1 molar ratio) and methylammonium bromide (1.09:1 molar ratio) powders respectively, to obtain $MAPbBr_3$ and $FAPbI_3$ solutions with a final concentration of 1.24 M. These two solutions are then mixed in a 17:83 volume ratio. Second, the cesium cation was added from a 1.5 M CsI solution in DMSO in a 5:95 volume ratio. The perovskite solution was spin-coated on top of the Li-doped TiO_2 using the following 2 step program: first was at 2000 rpm with 2000 rpm acceleration for 12 s, the second one was 6000 rpm with 2000 rpm acceleration for 23 s (program's total time is 35 s). After 30 s, 300 μL of anisole was dropped on the spinning substrate to promote fast solvent removal, forming a smooth and compact layer. After the spin-coating program, the perovskite-coated sample was annealed at 100 °C for 60 min. Spiro-OMETAD was the most celebrated HSL in the n-i-p configuration of the PSCs that was deposited on top of the perovskite layer. A 28.4 mM Spiro-OMETAD solution in chlorobenzene was doped with dopants named tBP, LiTFSI, and Co(III)TFSI to enhance its HSL properties. The molar ratio of the solution was 1 Spiro-OMETAD: 3.3 TBP:0.5 LiTFSI (from a 1.8 M stock solution in acetonitrile):0.05 Co(III)TFSI (from a 0.25 M stock solution in acetonitrile). The same dopants and ratio are used to dope 10 mM small molecule solutions in chlorobenzene, and all the solutions are filtered before depositing on top of the perovskite layer. After all the dopants were added to the HSL solution, the PTFE (0.2 μm) filter was used for eliminating aggregations or not solved materials before spin-coating. The HSLs are coated by spin-coating at 1800 rpm for 30 s and 200 rpm acceleration. After deposition of the HSLs, all substrates are transferred to the drybox with a 10% relative humidity, and they are stored there overnight. The FTO side of the substrates is

https://doi.org/10.1021/acs.chemmater.3c02231
Chem. Mater. XXXX, XXX, XXX−XXX

Table 1. Optical and Electrochemical Relevant Parameters for Spiro-OMeTAD, HL-22, and HL-31 in DCM solution[a]

HTMs	HOMO [a] (eV)	LUMO [a] (eV)	E_g (eV)	λ_{abs} (nm)	λ_{em} (nm)	λ_{edge} (nm)
Spiro-OMeTAD	−5.00	−2.05	3.07	375	442	404
HL-22	−4.83 (−4.75)	−2.76 (−2.78)	2.07	537	680	598
HL-31	−5.01 (−5.02)	−2.89 (−2.79)	2.12	530	660	584

[a]Values in parentheses are from DFT calculations.

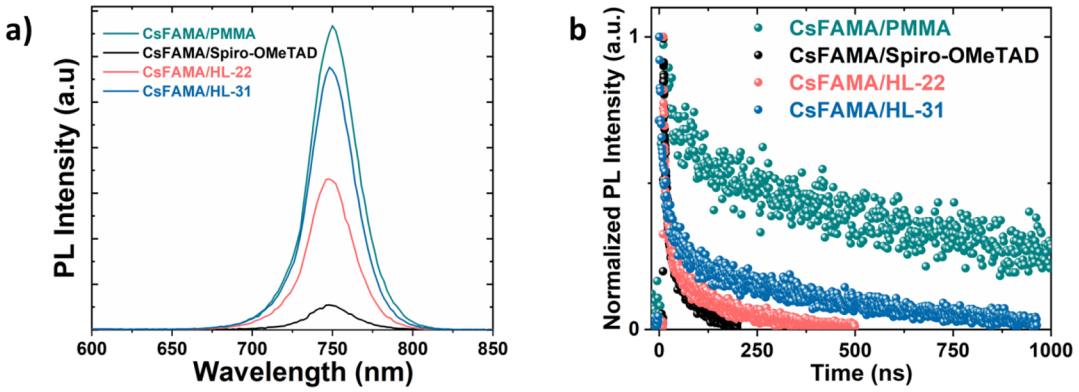

Figure 3. (a) Steady state photoluminescence (PL) spectra upon excitation at 470 nm. The perovskite and hole selective layers are prepared on top of the glass substrate. The PMMA film deposited on top of the perovskite serves as a moisture protective layer. (b) Time-correlated single photon counting measurements (TCSPC) of perovskite thin films with PMMA, **HL-22**, **HL-31**, and **Spiro-OMeTAD** deposited on top upon excitation at 470 nm and recorded at 750 nm.

cleaned with a sharp razor and a cotton swap with DMF before metal contact deposition on the following day.

The n-i-p configured perovskite devices are completed with 80 nm Au which was deposited using thermal evaporator under ultrahigh vacuum (1×10^{-6} mbar).

RESULTS AND DISCUSSION

Synthesis, Optical, and Electrochemical Characterization of the TIPS-Anthracene HTMs. The synthesis, depicted in Figure 1, of the two TIPS-anthracene-based HTMs is straightforward from 2,6-dibromo-TIPS-anthracene (**1**).[65] It relies on Suzuki cross-coupling reactions between compound (**1**) and the boronic ester (**2**) for **HL-31** and Buchwald–Hartwig amination between compound (**1**) and the commercially available compound (**3**) for **HL-22**. The synthesis of **HL-22** and **HL-31** is very straightforward, relying on the recrystallization of the products, and more convenient than the more complex synthesis of **Spiro-OMeTAD**, which notably requires a sublimation process.[41] In addition, the cost of the reagents required to synthesize **HL-22** and **HL-31** was analyzed[66] (see the Supporting Information), resulting in 300 and 320€/g, respectively, lower than that of commercial **Spiro-OMeTAD** (366.5€/g), although their synthesis has not been fully optimized.

Table 2. Fit Values for the Deconvolution of the Luminescence Decays in Figure 3 in ns

films	τ_1	τ_2
CsFAMA/PMMA	39.9	853.6
CsFAMA/Spiro-OMeTAD	7.4	73.0
CsFAMA/HL-22	6.6	115.0
CsFAMA/HL-31	15.0	361.8

Once the products were obtained, we set about characterizing their optoelectronic properties in order to compare them with those of **Spiro-OMeTAD**. Figure 2 illustrates the UV–visible spectra recorded in DCM solvent for **HL-22** and **HL-31** compared to those of **Spiro-OMeTAD** at room temperature. Compared with TIPS-anthracene, which exhibits a wavelength maximum at 441 nm, the two TIPS-anthracene derivatives show a pronounced charge transfer absorption band above 500 nm. **HL-31** and **HL-22** display wavelength maxima at 530 and 537 nm, respectively, with ε = 37600 and 8600 L mol^{-1} cm^{-1}, which is in clear contrast to **Spiro-OMeTAD** that barely absorbs beyond 420 nm. However, the increase of parasitic absorption in the visible range of **HL-31** and **HL-22** is not a matter of concern in n-i-p devices like the ones considered in this study, as the light reaches the absorbing layer from the ETM and not from the HTM,[67] unlike in p-i-n devices. When excited at the maximum wavelength of the charge transfer band, **HL-31** and **HL-22** emit light centered at 660 and 680 nm, respectively. Table 1 lists the optical properties of both anthracene-based hole transport materials as well as **Spiro-OMeTAD**.

Furthermore, with the aim to compare the energy levels of **HL-22** and **HL-31** with the ones of **Spiro-OMeTAD**, we carried out cyclic voltammetry measurements in dichloromethane using Fc/Fc$^+$ couple and evaluated the first oxidation potential that, together with the fluorescence emission measurements can give a valuable estimation for the HOMO (highest occupied molecular orbital) and the LUMO (lowest unoccupied molecular orbital) energy values. The measurement results are given in Table 1. Compared with **Spiro-OMeTAD**, **HL-31** has the same HOMO energy level of about −5.0 eV, while the HOMO energy level of **HL-22** is shifted to higher energy at about −4.8 eV. These results are in very good agreement with the ones of DFT calculations, with a HOMO found at −5.02 eV for **HL-31** and at −4.75 eV for **HL-22** (Figure S7). On the contrary, due to the TIPS-anthracene fragment, the LUMO energy levels are significantly shifted to lower energies at −2.76 and −2.89 eV for **HL-22** and **HL-31**, respectively, thus reducing the band gap compared to **Spiro-**

https://doi.org/10.1021/acs.chemmater.3c02231
Chem. Mater. XXXX, XXX, XXX−XXX

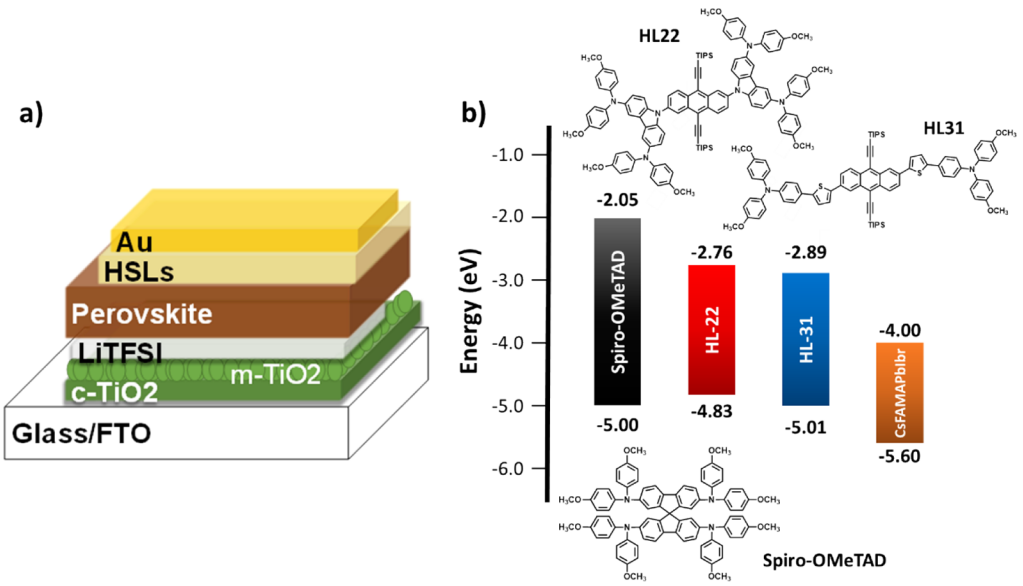

Figure 4. (a) Schematic representation of the used n-i-p device configuration for functional solar cells. (b) Schematic energy alignment between the perovskite material and three different HTMs.

OMeTAD. The HOMO and LUMO levels calculated via DFT are displayed in Figure S8. In both cases, the HOMO−LUMO are well separated, with the HOMO levels predominantly located on the triarylamine moieties and the LUMO on the anthracene core. From the estimation of the energy levels one should note that as for the **Spiro-OMeTAD**, the HOMO level of the new HTMs faces an important gap with the CsFAMA perovskite, whose valence band has an energy level of −5.60 eV.[62]

Thermogravimetric Analysis. The evaluation of the thermal behavior of the hole transport materials can give, in general, very good hints about the stability of the thin organic semiconductor film when incorporated into functional devices. This is of great importance in the case of perovskite solar cells using **Spiro-OMeTAD**, as the low glass transition temperature of this material[70,71] is responsible for the low thermal stability, one of the main current challenges for this kind of device.[72,73] Thermogravimetric analysis (TGA) and differential scanning calorimetry (DSC) are routine techniques for obtaining such experimental information. Figure S9 shows the TGA and DSC curves for **HL-22** and **HL-31**. The thermogravimetric and differential scanning calorimetry measurements for **HL-22** and **HL-31** were carried out under a N_2 atmosphere and with a fixed scan rate of 10 °C/min. In both cases, a 5% weight loss is observed at 430 and 440 °C for **HL-22** and **HL-31**, respectively. This weight loss value is formally attributed to the material decomposition at this temperature. For **Spiro-OMeTAD**, the decomposition temperature is 424 °C, slightly lower. From the DSC measurements, we can determine the glass transition temperature (T_g), which is obtained from the second cycle of the DSC. For **HL-22** T_g is found at 250 °C and at 254 °C for **HL-31**. These values are significantly higher than those reported for pristine **Spiro-OMeTAD** at about (121−124 °C)[71,72,74,75] and after the addition of LiTFSI and tBP these values are decreased (50−90 °C).[71,72,76]

Thin Films and Device Characterization. Once we had characterized the molecules, we proceeded to prepare thin films using triple-cation lead halide perovskite ($Cs_{0.05}FA_{0.79}MA_{0.16}Pb(I_{0.84}Br_{0.16})_3$;[60−62] FA stands for formamidinium; MA stands for methyl ammonium. We examined the steady-state photoluminescence (PL) properties of the perovskite film when the hole transport material is spin-coated onto the perovskite layer. The PL spectra of the bare perovskite film and the HTM-coated perovskite films were measured upon excitation at λ_{ex} = 470 nm. Figure 3 illustrates the differences in PL. The pristine perovskite thin film shows an emission peak maximum at λ_{em}= 750 nm in good agreement with previous literature reports.[60] A blue shift is observed upon superposition of the organic semiconductor thin film's superposition. Previous reports assigned this wavelength shift to the chemical interaction between the organic thin film and the perovskite material.[77,78]

The PL quenching for both CsFAMAPbIBr/**HL-22** and CsFAMAPbIBr/**HL-31** has a remarkable effect. On average, **HL-22** shows higher quenching of the perovskite PL. The PL quenching is closely related to the efficiency of the charge transfer process between the perovskite and the hole transport material.[21] In addition, to seek further information on the charge transfer dynamics between both materials, we carried out TCSPC measurements. To fairly compare between samples, a perovskite/PMMA thin film is used as a reference. The decay kinetics for the PL are shown in Figure 3 and the spectra were fitted according to the stretched exponential decay function.[79] A sample comparison shows that the CsFAMAPbIBr/**HL-22** film exhibits the shortest lifetime of 6.6 ns. Instead, for the CsFAMAPbIBr/**Spiro-OMeTAD** and CsFAMAPbIBr/**HL-31**, we recorded lifetimes of 7.4 and 15 ns, respectively. Overall, for CsFAMAPbIBr/**HL-22**, a comparable to **Spiro-OMeTAD** transfer kinetics in operando conditions is expected due to larger PL quenching and faster decay kinetics.[35] Table 2 lists the fitting values obtained from the decay deconvolution of the fluorescence emission decays.

Following the experiments to examine the properties of the hole transport materials, the hole mobility values were evaluated using the space-charge limited current (SCLC) method (see the Supporting Information).[80] Preliminary results (Table S3) showed that, as in the case of **Spiro-OMeTAD**, the efficiencies of the devices using the HTMs

https://doi.org/10.1021/acs.chemmater.3c02231
Chem. Mater. XXXX, XXX, XXX−XXX

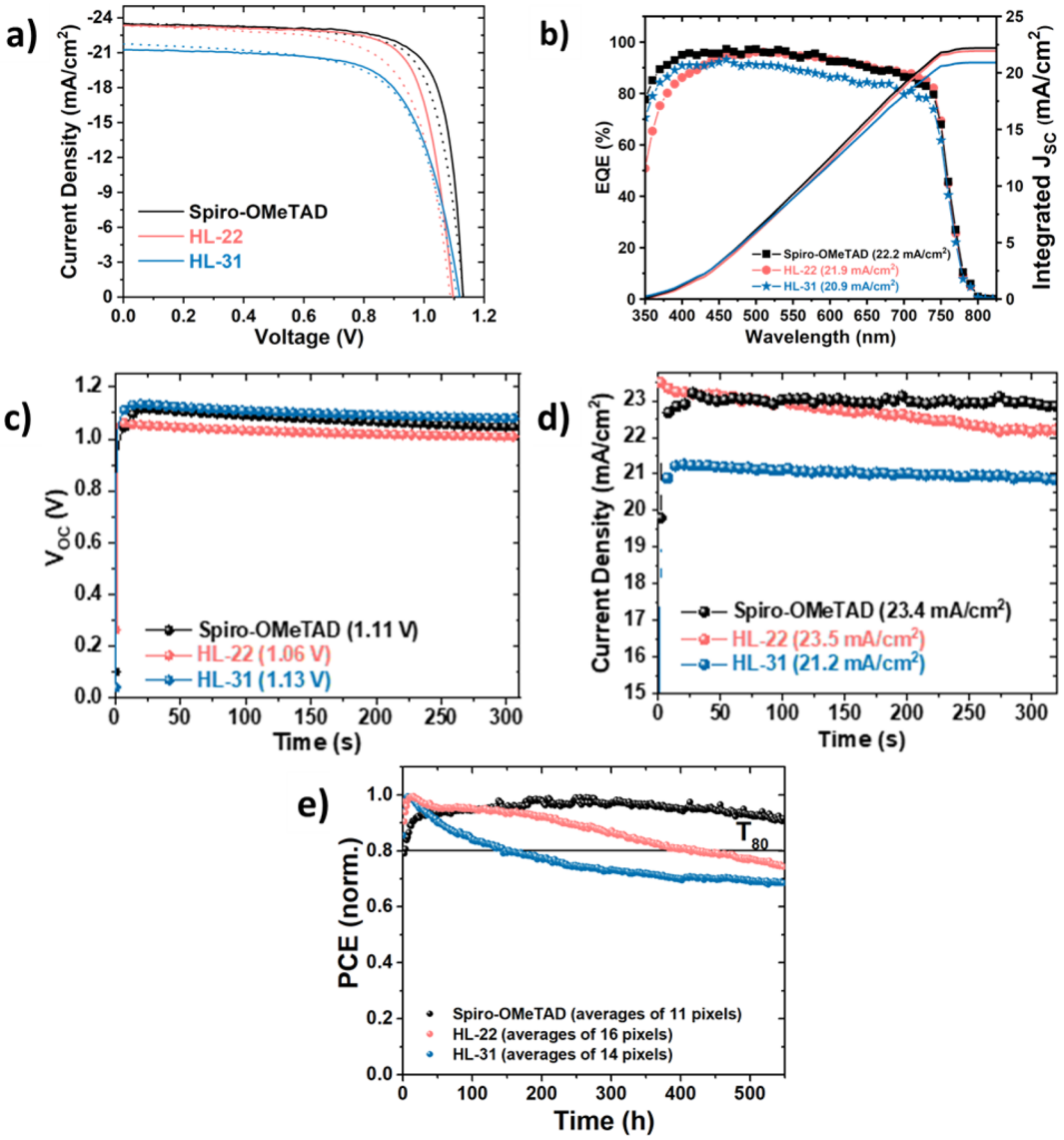

Figure 5. (a) $J-V$ curves for the devices based on **Spiro-OMeTAD**, **HL-22**, and **HL-31** with a scan rate of 40 mV/s. (b) Measured external quantum efficiency curves, which shows integrated current density in agreement with values from the $J-V$ measurements with the different hole transport materials. (c) Open circuit voltage (V_{OC}) and (d) J_{SC} (short circuit photocurrent) stability measurements for 350s under 1 sun illumination (100 mW/cm^2 1.5 AM G sun simulated spectra). (e) Solar cells maximum power point efficiency tracking for the different solar cells for over 500 h at 25 °C. The devices were measured under nitrogen without further encapsulation.

without dopants were low. For this reason, the organic semiconductor thin films were prepared under conditions identical to those prepared for efficient solar cells, including the chemical dopants (see the details in the Experimental Section). As a reference sample, **Spiro-OMeTAD** films were used, which show hole mobility values of $\mu = 2.7 \times 10^{-3} \pm 0.86$ cm^2 V^{-1} s^{-1} in agreement with those numbers reported in the scientific literature for **Spiro-OMeTAD** containing chemical dopants.[30,31] For the novel hole transport materials **HL-22** and **HL-31,** the mobility values (μ) were lower. **HL-22** exhibits hole mobility values of $\mu = 4.9 \times 10^{-4} \pm 1.65$ cm^{2}V^{-1}s^{-1} while **HL-31** displays values of $\mu = 3.0 \times 10^{-4} \pm 1.6$ cm^{2}V^{-1}s^{-1}, which are 1 order of magnitude lower than that for **Spiro-OMeTAD**. However, it is worth mentioning that the high mobility obtained for **Spiro-OMeTAD** is the result of an optimization process along the years of the chemical dopants,[30,34,35] while for the sake of comparison the same doping process is used for the novel materials (see Experimental Section), which is not necessary for the optimized procedure for these new materials.

The functional photovoltaic devices were prepared taking into account all of the above information with the following device structure: ITO/c-TiO$_2$/m-TiO$_2$/LiTFSI/CsFAMAP-bIBr/HTM/Au (see Figure 4a) with the band alignment between the perovskite and the different HTMs shown in Figure 4b. It is worthwhile to note that we have used the "one step" conventional method for the perovskite deposition that implies the antisolvent step (see Experimental Section). This step is critical to achieving a monolithic and homogeneous hybrid perovskite layer. We employed devices prepared using **Spiro-OMeTAD** as a standard for comparison purposes. Figure S11 illustrates a cross-section of the different device layers by using scanning electron microscopy (SEM).

Figure 5a shows that the hysteresis present in these devices is negligible and the obtained J_{SC} is in good agreement with the integrated J_{SC} extracted from IPCE in Figure 5b. In addition,

https://doi.org/10.1021/acs.chemmater.3c02231
Chem. Mater. XXXX, XXX, XXX−XXX

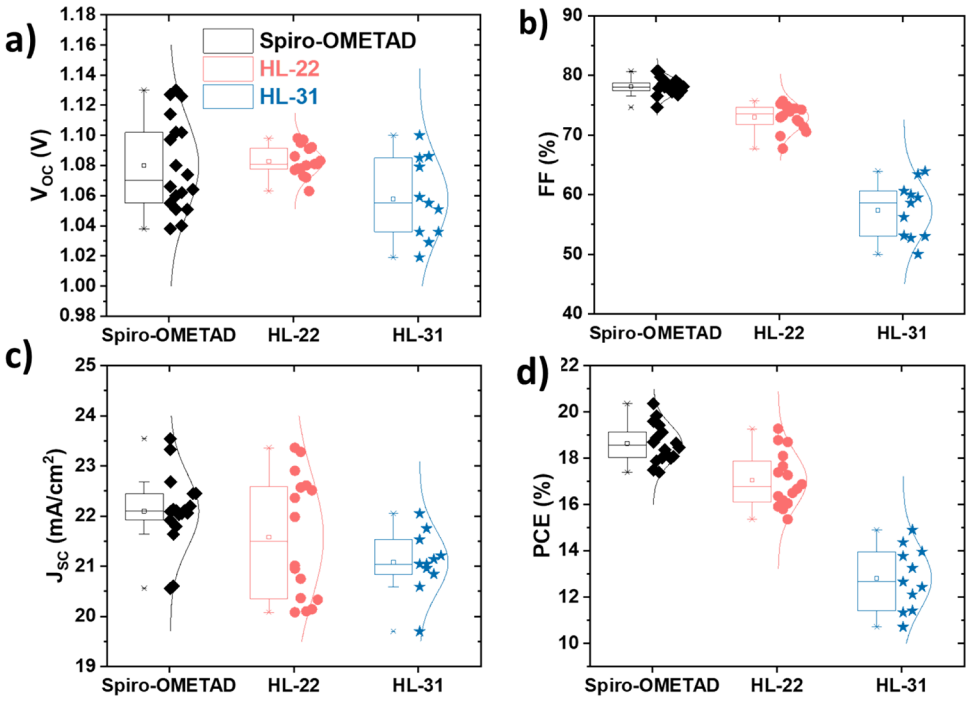

Figure 6. Statistics for the different parameters of the measured solar cells for **Spiro-OMeTAD**, **HL-22**, and **HL-31** based solar cells.

Table 3. Photovoltaic Parameters of the Best-Performance Perovskite Solar Cells Using Spiro-OMeTAD, HL-22, and HL-31 as HTM in Forward and Reverse Scans with a Scan Rate of 40 mV/s

materials	scan	J_{sc} (mA/cm^2)	V_{oc} (V)	FF	PCE (%)
Spiro-OMeTAD	reverse	23.5	1.130	0.76	20.3
	forward	23.4	1.132	0.74	19.7
HL-31	reverse	21.2	1.119	0.68	16.6
	forward	21.8	1.110	0.66	15.9
HL-22	reverse	23.3	1.097	0.75	19.2
	forward	23.3	1.088	0.69	17.6

Figures 5c–e also show that the devices are stable enough to perform the characterization, and the results are similar to those obtained for the **Spiro-OMeTAD** based devices.

Figure 6 collects the different statistical parameters for the measured solar cells, and the values for the best cells are given in Table 3. The different parameters' statistical distribution was achieved after measuring more than 10 solar cells for each hole transport material. Figure 6 shows how the solar cells based on **HL-22** offer higher fill factor (FF), open circuit voltage (V_{OC}), photocurrent density (J_{SC}), and efficiency (PCE) than solar cells based on **HL-31** and are almost at the same level as the **Spiro-OMeTAD**-based perovskite solar cells. The PCE obtained for the **Spiro-OMeTAD** reference is in agreement with the reported state-of-the-art using a similar perovskite.[31,81]

The three materials show similar J_{SC}, which is driven by the difference between the HOMO level of the HTMs and the valence band of the perovskite,[60,82−84] which decreases the hole injection, leading to charge accumulation at the interfaces, thus enhancing interfacial recombination.[39] This phenomenon is also responsible for the V_{OC} obtained, which is similar for the three materials. Hence, the differences in the PCE, are mostly linked to the fill factor (FF), which is best for the **Spiro-OMeTAD** devices and worst for **HL-31**, while **HL-22** has intermediate values. This follows the same pattern as that for the hole mobility reported for the three materials. Lower mobility, compared to the perovskite film, produces limits in the charge transit times,[85] which strongly affects the FF in perovskite solar cells.[85,86]

CONCLUSIONS

Overall, we have reported two novel HTMs, **HL-22** and **HL-31**, for use in PSCs with synthesis more straightforward than

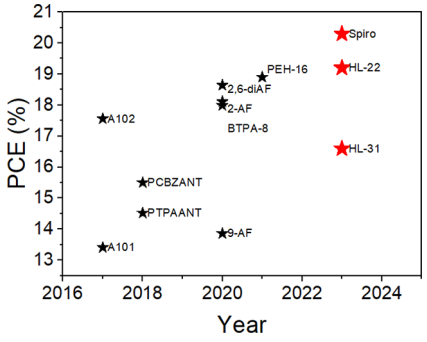

Figure 7. PCE evolution of perovskite solar cells using anthracene-based HTMs.[54,59,87−89] In red are the results reported in this work. Detailed photovoltaic parameters can be found in the Supporting Information.

that of **Spiro-OMeTAD**. Our results show that introducing TIPS substituents on anthracene-based HTMs is a good strategy to facilitate the purification of this class of molecules which are obtained by simple recrystallization. When tested in solar cells fabricated with the hybrid perovskite $(Cs_{0.05}FA_{0.79}MA_{0.16}Pb(I_{0.84}Br_{0.16})_3)$, one of the new molecules, **HL-22**, showed a PCE of 19.2% comparable to that of **Spiro-OMeTAD** (20.3%) and a T_{80} of around 400 h. Among the various anthracene-based HTMs reported in the literature to date, **HL-22** showed the highest PCE as shown in Figure 7. It

https://doi.org/10.1021/acs.chemmater.3c02231
Chem. Mater. XXXX, XXX, XXX−XXX

should be noted that the PCE for these new materials is limited by their FF, which may be related to their lower hole mobility compared to **Spiro-OMeTAD**. However, this aspect could be improved in the future by reoptimizing the chemical dopants and the thickness of the HTM layers.[90,91]

■ ASSOCIATED CONTENT

Supporting Information

The Supporting Information is available free of charge at https://pubs.acs.org/doi/10.1021/acs.chemmater.3c02231.

Detailed synthesis and characterization (NMR and mass spectrometry) of the molecules **HL-22** and **HL-31**, and analysis of the costs of the reagents involved in these synthesis, cyclic voltammetry results on these molecules and their geometry optimization by DFT calculations, thermogravimetric and SCLC results; SEM characterization and photovoltaic parameters of the solar devices fabricated using these molecules as HTMs; and a table comparing the results reported in this work with previous works from the literature reporting anthracene-based HTMs (PDF)

■ AUTHOR INFORMATION

Corresponding Authors

Renaud Demadrille − *Université Grenoble Alpes, CEA, CNRS, IRIG-SyMMES, Grenoble F-38000, France;* orcid.org/0000-0002-7455-5709; Email: renaud.demadrille@cea.fr

Emilio Palomares − *Institut Català d'Investigació Química (ICIQ-CERCA), Tarragona E-43007, Spain; ICREA, Barcelona E-08010, Spain;* orcid.org/0000-0002-5092-9227; Email: epalomares@ICIQ.ES

Authors

Ece Aktas − *Institut Català d'Investigació Química (ICIQ-CERCA), Tarragona E-43007, Spain;* Present Address: Department of Chemical, Materials, and Production Engineering, University of Naples Federico II, 80125 Fuorigrotta, Italy

Thi Huong Le − *Department of Advanced Materials Science and Nanotechnology, University of Science and Technology of Hanoi (USTH) Vietnam Academy of Science and Technology (VAST) 18 - Hoang Quoc Viet, Ha Noi 11307, Vietnam; Institut Lavoisier de Versailles, UMR CNRS 8180, Université Paris-Saclay, Versailles Cedex 78035, France;* Present Address: Department of Advanced Materials Science and Nanotechnology, University of Science and Technology of Hanoi (USTH) Vietnam Academy of Science and Technology (VAST) 18 - Hoang Quoc Viet, Cau Giay, Ha Noi 11307, Vietnam

Michel Frigoli − *Institut Lavoisier de Versailles, UMR CNRS 8180, Université Paris-Saclay, Versailles Cedex 78035, France;* orcid.org/0000-0001-5576-1868

Guixiang Li − *Helmholtz-Zentrum Berlin für Materialien und Energie GmbH, Berlin 14109, Germany;* orcid.org/0000-0002-8730-0713

Hans Köbler − *Helmholtz-Zentrum Berlin für Materialien und Energie GmbH, Berlin 14109, Germany*

Johan Liotier − *Université Grenoble Alpes, CEA, CNRS, IRIG-SyMMES, Grenoble F-38000, France;* orcid.org/0000-0003-1747-693X

Antonio J. Riquelme − *Université Grenoble Alpes, CEA, CNRS, IRIG-SyMMES, Grenoble F-38000, France;* orcid.org/0000-0003-2445-3664

Antonio Abate − *Helmholtz-Zentrum Berlin für Materialien und Energie GmbH, Berlin 14109, Germany*

Complete contact information is available at: https://pubs.acs.org/10.1021/acs.chemmater.3c02231

Author Contributions

T.H.L. and M.F.: design, synthesis, and characterization of the molecules (investigation-methodology-visualization). E.A, G.L., and H.K.: fabrication, characterization of the solar cells, and analysis of the results. J.L.: DFT calculation (investigation-methodology-visualization). R.D., E.P., and A.A. supervision of the work, analysis of the data and acquisition of financial support (conceptualization, funding acquisition, supervision, validation). E.A., A.R.E., E.P., and R.D.: curation of the data and writing of the manuscript (validation-writing-editing). The manuscript was written through contributions of all authors. All authors have given approval to the final version of the manuscript.

Funding

M.F. acknowledges financial support from the Agence Nationale de la Recherche Grant Number ANR-16-CE07−0024 (GATE). T.H.L. acknowledges the VAST project code THTETN.03/21−23 for funding. R.D. acknowledges the European Research Council (ERC) for funding. This work was funded under the European Union's Horizon 2020 research and innovation program (grant agreement number 832606; project PISCO).

Notes

The authors declare no competing financial interest.

■ REFERENCES

(1) Snaith, H. J. Perovskites: The Emergence of a New Era for Low-Cost, High-Efficiency Solar Cells. *J. Phys. Chem. Lett.* **2013**, *4* (21), 3623−3630.

(2) Green, M. A.; Ho-Baillie, A.; Snaith, H. J. The Emergence of Perovskite Solar Cells. *Nat. Photonics* **2014**, *8* (7), 506.

(3) Park, N.-G. Perovskite Solar Cells: An Emerging Photovoltaic Technology. *Mater. Today* **2015**, *18* (2), 65−72.

(4) Kim, H.-S.; Lee, C.-R.; Im, J.-H.; Lee, K.-B.; Moehl, T.; Marchioro, A.; Moon, S.-J.; Humphry-Baker, R.; Yum, J.-H.; Moser, J. E.; Grätzel, M.; Park, N.-G. Lead Iodide Perovskite Sensitized All-Solid-State Submicron Thin Film Mesoscopic Solar Cell with Efficiency Exceeding 9%. *Sci. Rep.* **2012**, *2*, 591 DOI: 10.1038/srep00591.

(5) Park, J.; Kim, J.; Yun, H.-S.; Paik, M. J.; Noh, E.; Mun, H. J.; Kim, M. G.; Shin, T. J.; Seok, S. I. Controlled Growth of Perovskite Layers with Volatile Alkylammonium Chlorides. *Nature* **2023**, *616* (7958), 724−730.

(6) NREL. *NREL: National Center for Photovoltaics Home Page*. March 2015. http://www.nrel.gov/ncpv/ (accessed 2015−03−05).

(7) Li, H.; Zhang, W. Perovskite Tandem Solar Cells: From Fundamentals to Commercial Deployment. *Chem. Rev.* **2020**, *120* (18), 9835−9950.

(8) Schulz, P.; Cahen, D.; Kahn, A. Halide Perovskites: Is It All about the Interfaces? *Chem. Rev.* **2019**, *119* (5), 3349−3417.

(9) Hermes, I. M.; Hou, Y.; Bergmann, V. W.; Brabec, C. J.; Weber, S. A. L. The Interplay of Contact Layers: How the Electron Transport Layer Influences Interfacial Recombination and Hole Extraction in Perovskite Solar Cells. *J. Phys. Chem. Lett.* **2018**, *9* (21), 6249−6256.

(10) Mahmood, K.; Sarwar, S.; Mehran, M. T. Current Status of Electron Transport Layers in Perovskite Solar Cells: Materials and Properties. *RSC Adv.* **2017**, *7* (28), 17044−17062.

(11) Juarez-Perez, E. J.; Wuβler, M.; Fabregat-Santiago, F.; Lakus-Wollny, K.; Mankel, E.; Mayer, T.; Jaegermann, W.; Mora-Sero, I. Role of the Selective Contacts in the Performance of Lead Halide Perovskite Solar Cells. *J. Phys. Chem. Lett.* **2014**, *5* (4), 680−685.
(12) Xu, W.; Hart, L. J. F.; Moss, B.; Caprioglio, P.; Macdonald, T. J.; Furlan, F.; Panidi, J.; Oliver, R. D. J.; Pacalaj, R. A.; Heeney, M.; Gasparini, N.; Snaith, H. J.; Barnes, P. R. F.; Durrant, J. R. Impact of Interface Energetic Alignment and Mobile Ions on Charge Carrier Accumulation and Extraction in P-i-n Perovskite Solar Cells. *Adv. Energy Mater.* **2023**, *13* (36), 2301102.
(13) Courtier, N. E.; Cave, J. M.; Foster, J. M.; Walker, A. B.; Richardson, G. How Transport Layer Properties Affect Perovskite Solar Cell Performance: Insights from a Coupled Charge Transport/Ion Migration Model. *Energy Environ. Sci.* **2019**, *12*, 396−409.
(14) Stolterfoht, M.; Caprioglio, P.; Wolff, C. M.; Márquez, J. A.; Nordmann, J.; Zhang, S.; Rothhardt, D.; Hörmann, U.; Amir, Y.; Redinger, A.; Kegelmann, L.; Zu, F.; Albrecht, S.; Koch, N.; Kirchartz, T.; Saliba, M.; Unold, T.; Neher, D. The Impact of Energy Alignment and Interfacial Recombination on the Internal and External Open-Circuit Voltage of Perovskite Solar Cells. *Energy Environ. Sci.* **2019**, *12* (9), 2778−2788.
(15) Roose, B.; Wang, Q.; Abate, A. The Role of Charge Selective Contacts in Perovskite Solar Cell Stability. *Adv. Energy Mater.* **2019**, *9* (5), 1803140.
(16) Sekimoto, T.; Matsui, T.; Nishihara, T.; Uchida, R.; Sekiguchi, T.; Negami, T. Influence of a Hole-Transport Layer on Light-Induced Degradation of Mixed Organic−Inorganic Halide Perovskite Solar Cells. *ACS Appl. Energy Mater.* **2019**, *2* (7), 5039−5049.
(17) Ravishankar, S.; Gharibzadeh, S.; Roldán-Carmona, C.; Grancini, G.; Lee, Y.; Ralaiarisoa, M.; Asiri, A. M.; Koch, N.; Bisquert, J.; Nazeeruddin, M. K. Influence of Charge Transport Layers on Open-Circuit Voltage and Hysteresis in Perovskite Solar Cells. *Joule* **2018**, *2* (4), 788−798.
(18) García-Rodríguez, R.; Riquelme, A. J.; Cowley, M.; Valadez-Villalobos, K.; Oskam, G.; Bennett, L. J.; Wolf, M. J.; Contreras-Bernal, L.; Cameron, P. J.; Walker, A. B.; Anta, J. A. Inverted Hysteresis in n−i−p and p−i−n Perovskite Solar Cells. *Energy Technol.* **2022**, *10* (12), 2200507.
(19) Hagfeldt, A.; Boschloo, G.; Sun, L.; Kloo, L.; Pettersson, H. Dye-Sensitized Solar Cells. *Chem. Rev.* **2010**, *110* (11), 6595−6663.
(20) Li, Y.; Huang, W.; Zhao, D.; Wang, L.; Jiao, Z.; Huang, Q.; Wang, P.; Sun, M.; Yuan, G. Recent Progress in Organic Solar Cells: A Review on Materials from Acceptor to Donor. *Molecules* **2022**, *27* (6), 1800.
(21) Xing, G.; Mathews, N.; Sun, S.; Lim, S. S.; Lam, Y. M.; Grätzel, M.; Mhaisalkar, S.; Sum, T. C. Long-Range Balanced Electron- and Hole-Transport Lengths in Organic-Inorganic CH3NH3PbI3. *Science* **2013**, *342* (6156), 344−347.
(22) Stranks, S. D.; Eperon, G. E.; Grancini, G.; Menelaou, C.; Alcocer, M. J. P.; Leijtens, T.; Herz, L. M.; Petrozza, A.; Snaith, H. J. Electron-Hole Diffusion Lengths Exceeding 1 Micrometer in an Organometal Trihalide Perovskite Absorber. *Science* **2013**, *342* (6156), 341−344.
(23) Deschler, F.; Price, M.; Pathak, S.; Klintberg, L. E.; Jarausch, D.-D.; Higler, R.; Hüttner, S.; Leijtens, T.; Stranks, S. D.; Snaith, H. J.; Atatüre, M.; Phillips, R. T.; Friend, R. H. High Photoluminescence Efficiency and Optically Pumped Lasing in Solution-Processed Mixed Halide Perovskite Semiconductors. *J. Phys. Chem. Lett.* **2014**, *5* (8), 1421−1426.
(24) Manser, J. S.; Christians, J. A.; Kamat, P. V. Intriguing Optoelectronic Properties of Metal Halide Perovskites. *Chem. Rev.* **2016**, *116* (21), 12956−13008.
(25) Tress, W. Perovskite Solar Cells on the Way to Their Radiative Efficiency Limit − Insights Into a Success Story of High Open-Circuit Voltage and Low Recombination. *Adv. Energy Mater.* **2017**, *7* (14), 1602358.
(26) Eames, C.; Frost, J. M.; Barnes, P. R. F.; O'Regan, B. C.; Walsh, A.; Islam, M. S. Ionic Transport in Hybrid Lead Iodide Perovskite Solar Cells. *Nat. Commun.* **2015**, *6*, 7497.
(27) Walsh, A. Principles of Chemical Bonding and Band Gap Engineering in Hybrid Organic−Inorganic Halide Perovskites. *J. Phys. Chem. C* **2015**, *119* (11), 5755−5760.
(28) Mesquita, I.; Andrade, L.; Mendes, A. Perovskite Solar Cells: Materials, Configurations and Stability. *Renew. Sustain. Energy Rev.***2018**. *822471*.
(29) Gholipour, S.; Saliba, M. From Exceptional Properties to Stability Challenges of Perovskite Solar Cells. *Small* **2018**, *14* (46), 1802385.
(30) Hawash, Z.; Ono, L. K.; Qi, Y. Recent Advances in Spiro-MeOTAD Hole Transport Material and Its Applications in Organic−Inorganic Halide Perovskite Solar Cells. *Adv. Mater. Interfaces* **2018**, *5* (1), 1700623.
(31) Nakka, L.; Cheng, Y.; Aberle, A. G.; Lin, F. Analytical Review of Spiro-OMeTAD Hole Transport Materials: Paths Toward Stable and Efficient Perovskite Solar Cells. *Adv. Energy Sustain. Res.* **2022**, *3* (8), 2200045.
(32) Tumen-Ulzii, G.; Matsushima, T.; Adachi, C. Mini-Review on Efficiency and Stability of Perovskite Solar Cells with Spiro-OMeTAD Hole Transport Layer: Recent Progress and Perspectives. *Energy Fuels* **2021**, *35* (23), 18915−18927.
(33) Abate, A.; Leijtens, T.; Pathak, S.; Teuscher, J.; Avolio, R.; Errico, M. E.; Kirkpatrik, J.; Ball, J. M.; Docampo, P.; McPherson, I.; Snaith, H. J. Lithium Salts as "Redox Active" p-Type Dopants for Organic Semiconductors and Their Impact in Solid-State Dye-Sensitized Solar Cells. *Phys. Chem. Chem. Phys.* **2013**, *15* (7), 2572−2579.
(34) Juarez-Perez, E. J.; Leyden, M. R.; Wang, S.; Ono, L. K.; Hawash, Z.; Qi, Y. Role of the Dopants on the Morphological and Transport Properties of Spiro-MeOTAD Hole Transport Layer. *Chem. Mater.* **2016**, *28* (16), 5702−5709.
(35) Rombach, F. M.; Haque, S. A.; Macdonald, T. J. Lessons Learned from Spiro-OMeTAD and PTAA in Perovskite Solar Cells. *Energy Environ. Sci.* **2021**, *14* (10), 5161−5190.
(36) Idígoras, J.; Aparicio, F. J.; Contreras-Bernal, L.; Ramos-Terrón, S.; Alcaire, M.; Sánchez-Valencia, J. R.; Borras, A.; Barranco, Á.; Anta, J. A. Enhancing Moisture and Water Resistance in Perovskite Solar Cells by Encapsulation with Ultrathin Plasma Polymers. *ACS Appl. Mater. Interfaces* **2018**, *10* (14), 11587−11594.
(37) Cheacharoen, R.; Rolston, N.; Harwood, D.; Bush, K. A.; Dauskardt, R. H.; McGehee, M. D. Design and Understanding of Encapsulated Perovskite Solar Cells to Withstand Temperature Cycling. *Energy Environ. Sci.* **2018**, *11* (1), 144−150.
(38) Caliò, L.; Salado, M.; Kazim, S.; Ahmad, S. A Generic Route of Hydrophobic Doping in Hole Transporting Material to Increase Longevity of Perovskite Solar Cells. *Joule* **2018**, *2* (9), 1800−1815.
(39) Ren, G.; Han, W.; Deng, Y.; Wu, W.; Li, Z.; Guo, J.; Bao, H.; Liu, C.; Guo, W. Strategies of Modifying Spiro-OMeTAD Materials for Perovskite Solar Cells: A Review. *J. Mater. Chem. A* **2021**, *9* (8), 4589−4625.
(40) Barranco, A.; Lopez-Santos, M. C.; Idigoras, J.; Aparicio, F. J.; Obrero-Perez, J.; Lopez-Flores, V.; Contreras-Bernal, L.; Rico, V.; Ferrer, J.; Espinos, J. P.; Borras, A.; Anta, J. A.; Sanchez-Valencia, J. R. Enhanced Stability of Perovskite Solar Cells Incorporating Dopant-Free Crystalline Spiro-OMeTAD Layers by Vacuum Sublimation. *Adv. Energy Mater.* **2020**, *10* (2), 1901524.
(41) Pham, H. D.; Wu, Z.; Ono, L. K.; Manzhos, S.; Feron, K.; Motta, N.; Qi, Y.; Sonar, P. Low-Cost Alternative High-Performance Hole-Transport Material for Perovskite Solar Cells and Its Comparative Study with Conventional SPIRO-OMeTAD. *Adv. Electron. Mater.* **2017**, *3* (8), 1700139.
(42) Shariatinia, Z. Recent Progress in Development of Diverse Kinds of Hole Transport Materials for the Perovskite Solar Cells: A Review. *Renew. Sustain. Energy Rev.* **2020**, *119*, 109608.
(43) Calió, L.; Kazim, S.; Grätzel, M.; Ahmad, S. Hole-Transport Materials for Perovskite Solar Cells. *Angew. Chem., Int. Ed.* **2016**, *55* (47), 14522−14545.
(44) Bakr, Z. H.; Wali, Q.; Fakharuddin, A.; Schmidt-Mende, L.; Brown, T. M.; Jose, R. Advances in Hole Transport Materials

https://doi.org/10.1021/acs.chemmater.3c02231
Chem. Mater. XXXX, XXX, XXX−XXX

Engineering for Stable and Efficient Perovskite Solar Cells. *Nano Energy* **2017**, *34*, 271−305.
(45) Zhang, C.; Wei, K.; Hu, J.; Cai, X.; Du, G.; Deng, J.; Luo, Z.; Zhang, X.; Wang, Y.; Yang, L.; Zhang, J. A Review on Organic Hole Transport Materials for Perovskite Solar Cells: Structure, *Composition and Reliability. Mater. Today***2023**. *67*518.
(46) Jegorovė, A.; Xia, J.; Steponaitis, M.; Daskeviciene, M.; Jankauskas, V.; Gruodis, A.; Kamarauskas, E.; Malinauskas, T.; Rakstys, K.; Alamry, K. A.; Getautis, V.; Nazeeruddin, M. K. Branched Fluorenylidene Derivatives with Low Ionization Potentials as Hole-Transporting Materials for Perovskite Solar Cells. *Chem. Mater.* **2023**, *35* (15), 5914−5923.
(47) Yeşil, T.; Mutlu, A.; Siyahjani Gültekin, S.; Günel, Z. G.; Zafer, C. Enhanced Hole Mobility of P-Type Materials by Molecular Engineering for Efficient Perovskite Solar Cells. *ACS Omega* **2023**, *8* (30), 27784−27793.
(48) Tsarev, S.; Yakushchenko, I. K.; Luchkin, S. Y.; Kuznetsov, P. M.; Timerbulatov, R. S.; Dremova, N. N.; Frolova, L. A.; Stevenson, K. J.; Troshin, P. A. A New Polytriarylamine Derivative for Dopant-Free High-Efficiency Perovskite Solar Cells. *Sustain. Energy Fuels* **2019**, *3* (10), 2627−2632.
(49) Yan, W.; Li, Y.; Li, Y.; Ye, S.; Liu, Z.; Wang, S.; Bian, Z.; Huang, C. Stable High-Performance Hybrid Perovskite Solar Cells with Ultrathin Polythiophene as Hole-Transporting Layer. *Nano Res.* **2015**, *8* (8), 2474−2480.
(50) Rodríguez-Seco, C.; Méndez, M.; Roldán-Carmona, C.; Pudi, R.; Nazeeruddin, M. K.; Palomares, E. J. Minimization of Carrier Losses for Efficient Perovskite Solar Cells through Structural Modification of Triphenylamine Derivatives. *Angew. Chem., Int. Ed.* **2020**, *59* (13), 5303−5307.
(51) Farokhi, A.; Shahroosvand, H.; Monache, G. D.; Pilkington, M.; Nazeeruddin, M. K. The Evolution of Triphenylamine Hole Transport Materials for Efficient Perovskite Solar Cells. *Chem. Soc. Rev.* **2022**, *51* (14), 5974−6064.
(52) Collavini, S.; Cabrera-Espinoza, A.; Delgado, J. L. Organic Polymers as Additives in Perovskite Solar Cells. *Macromolecules* **2021**, *54* (12), 5451−5463.
(53) Murugan, P.; Hu, T.; Hu, X.; Chen, Y. Advancements in Organic Small Molecule Hole-Transporting Materials for Perovskite Solar Cells: Past and Future. *J. Mater. Chem. A* **2022**, *10* (10), 5044−5081.
(54) Liu, X.; Kong, F.; Ghadari, R.; Jin, S.; Yu, T.; Chen, W.; Liu, G.; Tan, Z.; Chen, J.; Dai, S. Anthracene−Arylamine Hole Transporting Materials for Perovskite Solar Cells. *Chem. Commun.* **2017**, *53* (69), 9558−9561.
(55) Chen, M.; Yan, L.; Zhao, Y.; Murtaza, I.; Meng, H.; Huang, W. Anthracene-Based Semiconductors for Organic Field-Effect Transistors. *J. Mater. Chem. C* **2018**, *6* (28), 7416−7444.
(56) Huang, J.; Su, J.-H.; Tian, H. The Development of Anthracene Derivatives for Organic Light-Emitting Diodes. *J. Mater. Chem.* **2012**, *22* (22), 10977−10989.
(57) Dong, S.; Ong, A.; Chi, C. Photochemistry of Various Acene Based Molecules. *J. Photochem. Photobiol. C Photochem. Rev.* **2019**, *38*, 27−46.
(58) Marrocchi, A.; Silvestri, F.; Seri, M.; Facchetti, A.; Taticchi, A.; Marks, T. J. Conjugated Anthracene Derivatives as Donor Materials for Bulk Heterojunction Solar Cells: Olefinic versus Acetylenic Spacers. *Chem. Commun.* **2009**, *11*, 1380−1382.
(59) Singh, A.; Abate, S. Y.; Pavan Kumar, Ch.; Wu, W.-T.; Hsiao, J.-C.; Wu, F.-L.; Lin, J. T.; Tao, Y.-T. Bis(Diphenylamine)-Tethered Carbazolyl Anthracene Derivatives as Hole-Transporting Materials for Stable and High-Performance Perovskite Solar Cells. *ACS Appl. Energy Mater.* **2020**, *3* (11), 10752−10764.
(60) Saliba, M.; Matsui, T.; Seo, J. Y.; Domanski, K.; Correa-Baena, J. P.; Nazeeruddin, M. K.; Zakeeruddin, S. M.; Tress, W.; Abate, A.; Hagfeldt, A.; Grätzel, M. Cesium-Containing Triple Cation Perovskite Solar Cells: Improved Stability, Reproducibility and High Efficiency. *Energy Environ. Sci.* **2016**, *9* (6), 1989−1997.
(61) Raifuku, I.; Ishikawa, Y.; Chiang, Y.-H.; Lin, P.-Y.; Li, M.-H.; Uraoka, Y.; Chen, P. Segregation-Free Bromine-Doped Perovskite Solar Cells for IoT Applications. *RSC Adv.* **2019**, *9* (56), 32833−32838.
(62) Aktas, E.; Phung, N.; Köbler, H.; González, D. A.; Méndez, M.; Kafedjiska, I.; Turren-Cruz, S.-H.; Wenisch, R.; Lauermann, I.; Abate, A.; Palomares, E. Understanding the Perovskite/Self-Assembled Selective Contact Interface for Ultra-Stable and Highly Efficient p−i−n Perovskite Solar Cells. *Energy Environ. Sci.* **2021**, *14* (7), 3976−3985.
(63) Chun, D.; Cheng, Y.; Wudl, F. The Most Stable and Fully Characterized Functionalized Heptacene. *Angew. Chem., Int. Ed.* **2008**, *47* (44), 8380−8385.
(64) Li, S.; Yang, X.; Qu, D.; Wang, W.; Wang, Y.; Sun, L. Molecular Design of D-π-A Type II Organic Sensitizers for Dye Sensitized Solar Cells. *Chin. J. Chem.* **2012**, *30* (10), 2315−2321.
(65) Park, J.-H.; Chung, D. S.; Park, J.-W.; Ahn, T.; Kong, H.; Jung, Y. K.; Lee, J.; Yi, M. H.; Park, C. E.; Kwon, S.-K.; Shim, H.-K. Soluble and Easily Crystallized Anthracene Derivatives: Precursors of Solution-Processable Semiconducting Molecules. *Org. Lett.* **2007**, *9* (13), 2573−2576.
(66) Bettucci, O.; Pascual, J.; Turren-Cruz, S.; Cabrera-Espinoza, A.; Matsuda, W.; Völker, S. F.; Köbler, H.; Nierengarten, I.; Reginato, G.; Collavini, S.; Seki, S.; Nierengarten, J.; Abate, A.; Delgado, J. L. Dendritic-Like Molecules Built on a Pillar[5]Arene Core as Hole Transporting Materials for Perovskite Solar Cells. *Chem. - Eur. J.* **2021**, *27* (31), 8110−8117.
(67) Liu, T.; Chen, K.; Hu, Q.; Zhu, R.; Gong, Q. Inverted Perovskite Solar Cells: Progresses and Perspectives. *Adv. Energy Mater.* **2016**, *6* (17), 1600457.
(68) Wang, Q.; Smith, J. A.; Skroblin, D.; Steele, J. A.; Wolff, C. M.; Caprioglio, P.; Stolterfoht, M.; Kobler, H.; Li, M.; Turren-Cruz, S.-H.; Gollwitzer, C.; Neher, D.; Abate, A. Managing Phase Purities and Crystal Orientation for High-Performance and Photostable Cesium Lead Halide Perovskite Solar Cells. *Sol. RRL* **2020**, *4* (9), 2000213.
(69) Rakocevic, L.; Ernst, F.; Yimga, N. T.; Vashishtha, S.; Aernouts, T.; Heumueller, T.; Brabec, C. J.; Gehlhaar, R.; Poortmans, J. Reliable Performance Comparison of Perovskite Solar Cells Using Optimized Maximum Power Point Tracking. *Sol. RRL* **2019**, *3* (2), 1800287.
(70) Ren, Y.; Ren, M.; Xie, X.; Wang, J.; Cai, Y.; Yuan, Y.; Zhang, J.; Wang, P. A Spiro-OMeTAD Based Semiconductor Composite with over 100 °C Glass Transition Temperature for Durable Perovskite Solar Cells. *Nano Energy* **2021**, *81*, No. 105655.
(71) Malinauskas, T.; Tomkute-Luksiene, D.; Sens, R.; Daskeviciene, M.; Send, R.; Wonneberger, H.; Jankauskas, V.; Bruder, I.; Getautis, V. Enhancing Thermal Stability and Lifetime of Solid-State Dye-Sensitized Solar Cells via Molecular Engineering of the Hole-Transporting Material Spiro-OMeTAD. *ACS Appl. Mater. Interfaces* **2015**, *7* (21), 11107−11116.
(72) Jeong, S.-Y.; Kim, H.-S.; Park, N.-G. Challenges for Thermally Stable Spiro-MeOTAD toward the Market Entry of Highly Efficient Perovskite Solar Cells. *ACS Appl. Mater. Interfaces* **2022**, *14* (30), 34220−34227.
(73) Zhao, X.; Kim, H.-S.; Seo, J.-Y.; Park, N.-G. Effect of Selective Contacts on the Thermal Stability of Perovskite Solar Cells. *ACS Appl. Mater. Interfaces* **2017**, *9* (8), 7148−7153.
(74) Salbeck, J.; Weissörtel, F.; Bauer, J. Spiro Linked Compounds for Use as Active Materials in Organic Light Emitting Diodes. *Macromol. Symp.* **1998**, *125* (1), 121−132.
(75) Bach, U.; Lupo, D.; Comte, P.; Moser, J. E.; Weissörtel, F.; Salbeck, J.; Spreitzer, H.; Grätzel, M. Solid-State Dye-Sensitized Mesoporous TiO 2 Solar Cells with High Photon-to-Electron Conversion Efficiencies. *Nature* **1998**, *395* (6702), 583.
(76) Seo, J.-Y.; Kim, H.-S.; Akin, S.; Stojanovic, M.; Simon, E.; Fleischer, M.; Hagfeldt, A.; Zakeeruddin, S. M.; Grätzel, M. Novel P-Dopant toward Highly Efficient and Stable Perovskite Solar Cells. *Energy Environ. Sci.* **2018**, *11* (10), 2985−2992.
(77) Tress, W.; Marinova, N.; Inganäs, O.; Nazeeruddin, M. K.; Zakeeruddin, S. M.; Graetzel, M. The Role of the Hole-Transport

https://doi.org/10.1021/acs.chemmater.3c02231
Chem. Mater. XXXX, XXX, XXX−XXX

Layer in Perovskite Solar Cells - Reducing Recombination and Increasing Absorption. *2014 IEEE 40th Photovoltaic Specialist Conference (PVSC)* **2014**, 1563−1566.
(78) Rakstys, K.; Abate, A.; Dar, M. I.; Gao, P.; Jankauskas, V.; Jacopin, G.; Kamarauskas, E.; Kazim, S.; Ahmad, S.; Grätzel, M.; Nazeeruddin, M. K. Triazatruxene-Based Hole Transporting Materials for Highly Efficient Perovskite Solar Cells. *J. Am. Chem. Soc.* **2015**, *137* (51), 16172−16178.
(79) Aktas, E.; Jiménez-López, J.; Rodríguez-Seco, C.; Pudi, R.; Ortuño, M. A.; López, N.; Palomares, E. Supramolecular Coordination of Pb2+ Defects in Hybrid Lead Halide Perovskite Films Using Truxene Derivatives as Lewis Base Interlayers. *ChemPhysChem* **2019**, *20* (20), 2702−2711.
(80) Mihailetchi, V. D.; Wildeman, J.; Blom, P. W. M. Space-Charge Limited Photocurrent. *Phys. Rev. Lett.* **2005**, *94* (12), No. 126602.
(81) Du, Q.; Shen, Z.; Chen, C.; Li, F.; Jin, M.; Li, H.; Dong, C.; Zheng, J.; Ji, M.; Wang, M. Spiro-OMeTAD:Sb2S3 Hole Transport Layer with Triple Functions of Overcoming Lithium Salt Aggregation, Long-Term High Conductivity, and Defect Passivation for Perovskite Solar Cells. *Sol. RRL* **2021**, *5* (11), 2100622.
(82) Li, C.; Wei, J.; Sato, M.; Koike, H.; Xie, Z.-Z.; Li, Y.-Q.; Kanai, K.; Kera, S.; Ueno, N.; Tang, J.-X. Halide-Substituted Electronic Properties of Organometal Halide Perovskite Films: Direct and Inverse Photoemission Studies. *ACS Appl. Mater. Interfaces* **2016**, *8* (18), 11526−11531.
(83) Lee, J.-W.; Kim, D.-H.; Kim, H.-S.; Seo, S.-W.; Cho, S. M.; Park, N.-G. Formamidinium and Cesium Hybridization for Photo- and Moisture-Stable Perovskite Solar Cell. *Adv. Energy Mater.* **2015**, *5* (20), 1501310.
(84) Park, B.; Philippe, B.; Jain, S. M.; Zhang, X.; Edvinsson, T.; Rensmo, H.; Zietz, B.; Boschloo, G. Chemical Engineering of Methylammonium Lead Iodide/Bromide Perovskites: Tuning of Opto-Electronic Properties and Photovoltaic Performance. *J. Mater. Chem. A* **2015**, *3* (43), 21760−21771.
(85) Grill, I.; Aygüler, M. F.; Bein, T.; Docampo, P.; Hartmann, N. F.; Handloser, M.; Hartschuh, A. Charge Transport Limitations in Perovskite Solar Cells: The Effect of Charge Extraction Layers. *ACS Appl. Mater. Interfaces* **2017**, *9* (43), 37655−37661.
(86) Le Corre, V. M.; Stolterfoht, M.; Perdigón Toro, L.; Feuerstein, M.; Wolff, C.; Gil-Escrig, L.; Bolink, H. J.; Neher, D.; Koster, L. J. A. Charge Transport Layers Limiting the Efficiency of Perovskite Solar Cells: How To Optimize Conductivity, Doping, and Thickness. *ACS Appl. Energy Mater.* **2019**, *2* (9), 6280−6287.
(87) Paek, S. Novel Anthracene HTM Containing TIPs for Perovskite Solar Cells. *Processes* **2021**, *9* (12), 2249.
(88) Wu, G.; Zhang, Y.; Kaneko, R.; Kojima, Y.; Islam, A.; Sugawa, K.; Otsuki, J.; Liu, S. Facile Synthesis of "Lucky Clover" Hole-Transport Material for Efficient and Stable Large-Area Perovskite Solar Cells. *J. Power Sources* **2020**, *454*, No. 227938.
(89) Tong, T.; Tan, C.; Keller, T.; Li, B.; Zheng, C.; Scherf, U.; Gao, D.; Huang, W. Two Anthracene-Based Copolymers as the Hole-Transporting Materials for High-Performance Inverted (p-i-n) Perovskite Solar Cells. *Macromolecules* **2018**, *51* (18), 7407−7416.
(90) Marinova, N.; Tress, W.; Humphry-Baker, R.; Dar, M. I.; Bojinov, V.; Zakeeruddin, S. M.; Nazeeruddin, M. K.; Grätzel, M. Light Harvesting and Charge Recombination in CH3NH3PbI3 Perovskite Solar Cells Studied by Hole Transport Layer Thickness Variation. *ACS Nano* **2015**, *9* (4), 4200−4209.
(91) Kim, G.-W.; Shinde, D. V.; Park, T. Thickness of the Hole Transport Layer in Perovskite Solar Cells: Performance versus Reproducibility. *RSC Adv.* **2015**, *5* (120), 99356−99360.

https://doi.org/10.1021/acs.chemmater.3c02231
Chem. Mater. XXXX, XXX, XXX−XXX